Incoherence in bilayer systems with strong electronic correlations

2000 J. Phys.: Condens. Matter 12 2245

(http://iopscience.iop.org/0953-8984/12/10/309)

J. Phys.: Condens. Matter **12** (2000) 2245–2263. Printed in the UK PII: S0953-8984(00)04079-0

Incoherence in bilayer systems with strong electronic correlations

Werner Heindl, Thomas Pruschke and Joachim Keller

Institut für Theoretische Physik, Universität Regensburg, Universitätsstrasse 31, 93053 Regensburg, Germany

Received 7 May 1999, in final form 15 November 1999

Abstract. We present results for the one-particle properties and c-axis transport for exchange-coupled bilayer systems with strong electronic correlations in the paramagnetic phase. The model is solved within the dynamical mean-field theory (DMFT). By considering an effective two-site impurity we are able to treat the coupling between the layers in the diagonalization of the effective impurity exactly. The one-particle properties and the optical conductivity between the planes are studied, giving insight into a possible suppression of the one-particle hopping between the planes by the antiferromagnetic coupling. A strong renormalization of the bilayer splitting up to a complete suppression by the antiferromagnetic coupling is found. In the optical conductivity a strong blocking of the charge dynamics between the planes can be seen, accompanied by a low-energy excitation which must be attributed to inter-plane spin fluctuations.

1. Introduction

Most of the normal-state properties of the high-T_c superconductors can be qualitatively described by the Hubbard model [1] or the t–J model [2–5]. Here it is assumed that the electronic degrees of freedom which are responsible for transport, optical properties etc are essentially two-dimensional, and effectively consisting of copper $d_{x^2-y^2}$ orbitals. Electrons in these orbitals are usually subject to a particularly strong local Coulomb interaction leading to the experimentally observed anomalous properties.

The standard high-T_c material $(La, Sr)_2CuO_4$ indeed consists of single CuO_2 sheets well separated by insulating layers, and such a description seems to be justified. However, the compounds with the highest T_c are known to rather have stacks of two ($YBa_2Cu_3O_{6+\delta}$) or more ($Tl_2Ba_2Ca_2Cu_3O_{10}$) coupled CuO_2 planes separated by insulating layers.

There are several indications that the inter-layer coupling within these stacks of CuO_2 planes is crucial for understanding the electronic properties including superconductivity. Especially in the inter-layer tunnelling theory, the suppression of the coherent one-particle hopping between the CuO_2 layers in the normal state is the key point in moving towards an understanding of the mechanism of high-temperature superconductivity [6].

Such a suppression of coherence should have strong effects on physical quantities like one-particle excitations and the optical conductivity. For $YBa_2Cu_3O_{6+\delta}$ strong evidence for a bilayer splitting of the CuO_2 bands related to the existence of two CuO_2 planes in a unit cell can be found in photoemission experiments [8,9], whereas in $Bi_2Sr_2CaCu_2O_{8+\delta}$ only one band can be resolved experimentally [10, 11]. The optical conductivity perpendicular to the planes is found to be weak and incoherent in the normal state [12] of $YBa_2Cu_3O_{6.70}$.

0953-8984/00/102245+19$30.00

Effects caused by the multi-layer structure of the high-T_c materials can be investigated by suitable extensions of the two-dimensional Hubbard or t–J models. The bilayer Hubbard model was especially extensively studied, within the so-called fluctuation exchange (FLEX) approximation [13–15], where evidence was found that inter-layer antiferromagnetic correlations strongly reduce the one-particle hopping between the layers. However, this approximation is limited to values of the interaction between the relevant d states small compared to the bandwidth and a confirmation of such results from a different type of approach is clearly necessary.

The aim of this paper is to investigate the particular influence of the inter-layer antiferromagnetic correlations on the single-particle and optical properties in some detail. To this end we study a bilayer system, where electronic correlations in each layer are described by a Hubbard model in the limit of a very strong local Coulomb interaction $U \to \infty$. The two layers are coupled by a tight-binding and an antiferromagnetic exchange interaction. Special attention is paid to an accurate treatment of the inter-layer coupling.

The paper is organized as follows. The model and the method that we use to study it will be presented in section 2. Section 3 is devoted to the discussion of the single-particle properties of the model, which show a pronounced reduction of inter-plane coherence on increasing the inter-layer antiferromagnetic coupling. These findings are further confirmed by our results for the optical conductivity perpendicular to the planes presented in section 4. A summary and discussion will conclude the paper.

2. Method

As a model Hamiltonian for the two individual CuO_2 planes (enumerated with $l = 1, 2$) we use the standard $U = \infty$ Hubbard model [5], which is given by

$$H_l = (\epsilon_0 - \mu) \sum_i n_{l,i} - t \sum_{\langle ij \rangle, \sigma} \tilde{c}^\dagger_{l,\sigma,i} \tilde{c}_{l,\sigma,j}. \tag{1}$$

The operators $\tilde{c}^\dagger_{l,i,\sigma}$ create a particle at site i on layer l in the restricted Hilbert space of no doubly occupied lattice sites, $\boldsymbol{S}_{l,i}$ is the spin operator at site i on layer l and the corresponding occupation numbers are

$$n_{l,i} = \sum_\sigma \tilde{c}^\dagger_{l,\sigma,i} \tilde{c}_{l,\sigma,i}.$$

The coupling between the two layers is described by a hopping integral $t_\perp$ and an antiferromagnetic coupling $J_\perp$ arising in the standard way from virtual charge fluctuations between the layers. The inclusion of the latter interaction is very important, as neutron scattering experiments on YBaCuO show that antiferromagnetic correlations between the layers are very strong [16]. Thus, the inter-layer coupling is modelled by the Hamiltonian

$$H_{t_\perp} = -t_\perp \sum_{i,\sigma} (\tilde{c}^\dagger_{1,\sigma,i} \tilde{c}_{2,\sigma,i} + \tilde{c}^\dagger_{2,\sigma,i} \tilde{c}_{1,\sigma,i}) \tag{2}$$

$$H_{J_\perp} = -J_\perp \sum_i (\boldsymbol{S}_{1,i} \cdot \boldsymbol{S}_{2,i} - \frac{1}{4} n_{1,i} n_{2,i}) \tag{3}$$

and the complete model for describing the system of two coupled planes is finally given by

$$H = H_1 + H_2 + H_{t_\perp} + H_{J_\perp}. \tag{4}$$

In this paper we solve this model within the dynamical mean-field theory (DMFT) [17,18], which will now be suitably extended for the case of two coupled, correlated systems. The

non-interacting system is diagonal in the band picture of symmetric $a_{+,\sigma}(\boldsymbol{k})$ and antisymmetric $a_{-,\sigma}(\boldsymbol{k})$ fermion operators:

$$\begin{pmatrix} a_{+,\sigma}(\boldsymbol{k}) \\ a_{-,\sigma}(\boldsymbol{k}) \end{pmatrix} = \frac{1}{\sqrt{2}} \begin{pmatrix} +1 & +1 \\ +1 & -1 \end{pmatrix} \begin{pmatrix} c_{1,\sigma}(\boldsymbol{k}) \\ c_{2,\sigma}(\boldsymbol{k}) \end{pmatrix} \tag{5}$$

corresponding to a diagonal unperturbed Green's function:

$$\underline{\underline{G}}_{(0)}(\boldsymbol{k}, z) = \begin{pmatrix} z - \epsilon_{\boldsymbol{k}} - \epsilon_+ & 0 \\ 0 & z - \epsilon_{\boldsymbol{k}} - \epsilon_- \end{pmatrix}^{-1}. \tag{6}$$

Here a convenient matrix notation was introduced and $\boldsymbol{k}$ denotes the wave vector parallel to the layers. The energies $\epsilon_\pm$ are given by the expression $\epsilon_\pm = \epsilon_0 \mp t_\perp$. The full Green's function of the interacting system can be obtained in standard fashion through Dyson's equation

$$\underline{\underline{G}}^{-1}(\boldsymbol{k}, z) = \underline{\underline{G}}^{-1}_{(0)}(\boldsymbol{k}, z) - \underline{\underline{\Sigma}}(\boldsymbol{k}, z). \tag{7}$$

In the spirit of the DMFT we will neglect the $\boldsymbol{k}$-dependence of the self-energies *within each layer*.

This assumption can be justified in the limit of infinite coordination number, or spatial dimension d, respectively. To obtain a non-trivial model in this limit one has to scale the hopping matrix element as $t = t^*/(2\sqrt{d})$ [17, 18, 21]. Here we use the DMFT as an approximation even for $d = 2$. We will set $t^* = 1$ as the unit of energy and measure all energies relative to the chemical potential μ. For all numerical calculations we will use a model density of states for the non-interacting electron system of the form $\rho_0(\epsilon) = \pi^{-1/2} \exp(-\epsilon^2)$.

At this point we want to note that we introduce explicitly an exchange interaction $J_\perp$ between the layers but neglect the corresponding exchange interaction within the layers. A t–J model description for the layers would certainly be more realistic. The $U = \infty$ Hubbard model used instead nevertheless describes rather well the electronic correlations in the layers for the single-particle excitations. In the framework of the DMFT it is in fact equivalent to the t–J model in the paramagnetic state, because in this approximation the exchange interaction enters only at the Hartree level and hence contributes only in a magnetically ordered state. The inclusion of short-range magnetic fluctuations in the layers would require an extension of the DMFT to clusters as local units which in principle is possible. From experimental evidence and results obtained with other theoretical techniques it seems clear that at least in the paramagnetic phase the inter-layer coupling is the more important one with respect to a possible suppression of inter-layer coherence, and thus the neglect of the intra-layer exchange interactions seems to be justified for the time being.

Due to the low dimensionality of the coupling between the two layers—i.e. every lattice site on one layer is only connected to one lattice site on the opposite layer—the $k_\perp$-dependence of the self-energies perpendicular to the planes is treated exactly, giving two self-energies $\Sigma_{+/-}(z)$ corresponding to $k_\perp = 0$ and $k_\perp = \pi$.

Since the full Hamiltonian is symmetric under the exchange of the planes, the self-energy has two independent contributions

$$\underline{\underline{\Sigma}}(z) = \begin{pmatrix} \Sigma_+(z) & 0 \\ 0 & \Sigma_-(z) \end{pmatrix} \tag{8}$$

only, if we assume that there is no spontaneous symmetry breaking.

Finally, the local nature of the self-energies $\Sigma_+(z)$ and $\Sigma_-(z)$ allows one to map the lattice model onto an effective Anderson impurity problem. Motivated by the symmetry of the model we choose the effective impurity to consist of two adjacent lattice sites on the two layers. This choice allows us to treat the coupling between the layers exactly. We thus define the effective

impurity to be $H_{t_\perp} + H_{J_\perp}$. Diagonalizing this system gives (in the reduced Hilbert space without doubly occupied sites) nine eigenstates which are listed in table 1.

The crucial point here is the splitting of the two-particle states into a singlet state $|S = 0\rangle$ with an energy $2\epsilon_0 - J_\perp$ and a triplet state $|S = 1\rangle$ with energy $2\epsilon_0$. Note that both states are degenerate for $J_\perp = 0$ while the singlet has the lower energy for $J_\perp > 0$, as expected.

Table 1. Eigenstates of the effective impurity.

Number	Degeneracy	Name	Energy	Spin
0	1	$\|0\rangle$	0	0
1	2	$\|-, \sigma\rangle$	ϵ_-	$\frac{1}{2}$
1	2	$\|+, \sigma\rangle$	ϵ_+	$\frac{1}{2}$
2	3	$\|S = 1\rangle$	$2\epsilon_0$	1
2	1	$\|S = 0\rangle$	$2\epsilon_0 - J_\perp$	0

Within the DMFT the effective impurity couples to the remainder of the lattice through a 'Weiss field' $\Delta(\omega)$ which can be viewed as an average *dynamic* scattering potential for the local particles and replaces Anderson's hybridization function in the conventional single-impurity Anderson model. For a given self-energy $\Sigma_\alpha(z)$, where $\alpha = \pm$, and a corresponding local Green's function

$$G_\alpha(z) = \int \mathrm{d}\epsilon\ \rho_0(\epsilon) \frac{1}{z - \epsilon_\alpha - \epsilon - \Sigma_\alpha(z)} \tag{9}$$

the quantity $\Delta_\alpha(\omega)$ is obtained as [20, 26]

$$\Delta_\alpha(\omega) = \mathrm{Im}(G_\alpha(z)^{-1} + \Sigma_\alpha(z)). \tag{10}$$

As in a conventional mean-field theory, $\Delta_\alpha(\omega)$ has to be determined self-consistently in the course of the calculation.

The remaining problem is to solve the impurity problem defined by the set of states in table 1 and the given hybridization functions $\Delta_\alpha(\omega)$. Since we are dealing with a model at $U = \infty$, the only feasible method available up to now is the resolvent technique [22, 23], which represents a perturbation theory in $\Delta_\alpha(\omega)$. A well established approximation in this technique is the non-crossing approximation [24]. The resolvent approach together with the NCA has proven to be reliable and accurate in the one-band Hubbard model [19, 26, 27] and a suitable extension to multi-band systems has been worked out recently [28–30]. The subtle difference between these cases and the bilayer model under consideration is that there are two independent hybridization functions $\Delta_\alpha(\omega)$ present here. On the one hand, this difference is in particular important for obtaining non-trivial changes in the behaviour of the bilayer model as compared to the conventional t–J model. On the other hand, it leads to subtleties in the perturbation theory in the limit $t_\perp \to 0$, $J_\perp \to 0$ whose implications will be discussed in some detail in the appendix.

3. One-particle properties

Let us start the discussion of our results by examining the general structures of the density of states (DOS) as obtained from the local Green's functions via

$$\rho_\alpha(\omega) = -\frac{1}{\pi} \mathrm{Im}\, G_\alpha(\omega + \mathrm{i}\delta).$$

For $t_\perp = 0$ and $J_\perp = 0$ the model reduces to the usual one-band Hubbard model at $U = \infty$, whose dynamic properties in the paramagnetic phase have been studied extensively within DMFT [25, 26, 32]. There one obtains a so-called lower Hubbard band centred around ϵ_0 and a sharp quasi-particle peak at the Fermi level due to many-body effects. Since we are dealing with $U = \infty$ the upper Hubbard band is shifted to infinite energies.

In figure 1 the single-particle DOS for the symmetric ($\rho_+(\omega)$) and the antisymmetric ($\rho_-(\omega)$) states of the bilayer model with $t_\perp = 0.2$ and $J_\perp = 0.0$ at a temperature $T = 1/50$ is shown.

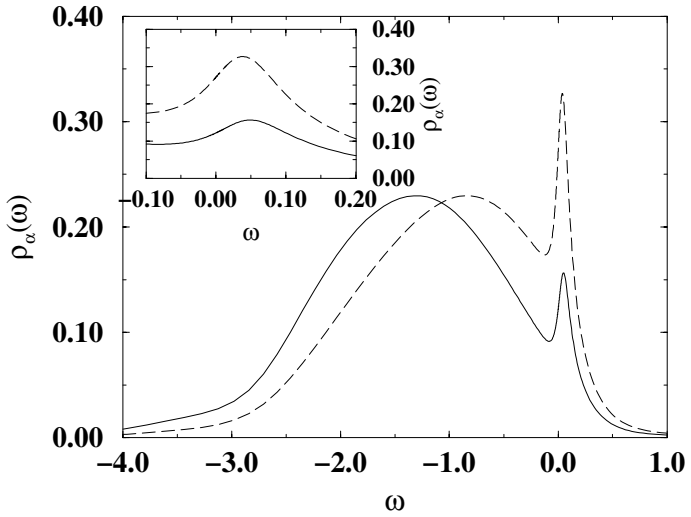

Figure 1. Spectral functions for the symmetric band (solid line) and antisymmetric band (dashed line) with parameters $J_\perp = 0$, $t_\perp = 0.2$, $\beta = 50.0$. The inset shows the region around the Fermi level.

One can clearly see the expected splitting of the lower Hubbard bands of the order of $2t_\perp$, with the symmetric band centred around $\epsilon_0 - t_\perp$ and the antisymmetric band around $\epsilon_0 + t_\perp$.

Since at low temperatures the physics is dominated by the behaviour at the Fermi level, we now concentrate on the effects of $t_\perp$ on the quasi-particle peak. The first observation that one makes here is that the height and width of the peaks for the symmetric and antisymmetric states are different, pointing towards different characteristic energy scales. From previous studies it is known that the quasi-particle peak has an origin similar to the Abrikosov–Suhl resonance [26, 27] well known from the physics of the single-impurity Anderson model. The scale for the development of this many-body resonance is set by the Kondo temperature, which obeys an exponential law of the form $\ln(T_K) \propto -|\epsilon_0|$. Assuming that this relation for the Kondo temperature can be applied here, too, we find two distinct Kondo temperatures $\ln(T_K^\pm) \propto -|\epsilon_\pm|$ for the two bands. With the other quantities entering T_K roughly taken as constant, we consequently should expect that $T_K^+ < T_K^-$. The width of the Kondo peak on the other hand scales as T_K which explains why the quasi-particle peak of the symmetric band is broader than the peak of the antisymmetric band. Moreover, for a given finite temperature the system with the larger T_K is closer to saturation and thus displays a higher peak, in accordance with figure 1.

In addition to the occurrence of two different energy scales for the symmetric and antisymmetric states, one also sees a splitting in the position of the maxima of the two resonances. Interestingly the direction of the shift is reversed as compared to the case for

the Hubbard bands: the quasi-particle peak for the symmetric band is shifted towards higher energies, while the one for the antisymmetric band has the lower energy. Also, the scale of this splitting is quite different from the bare inter-layer coupling $t_\perp$.

The influence of the correlations on the inter-layer hopping can be studied best by looking at the difference in energy ΔE of the maxima of the lower Hubbard bands, which for non-interacting particles should be just $2t_\perp$. The splitting of the maxima of the calculated DOS normalized to $2t_\perp$ as a function of $t_\perp$ is presented in figure 2.

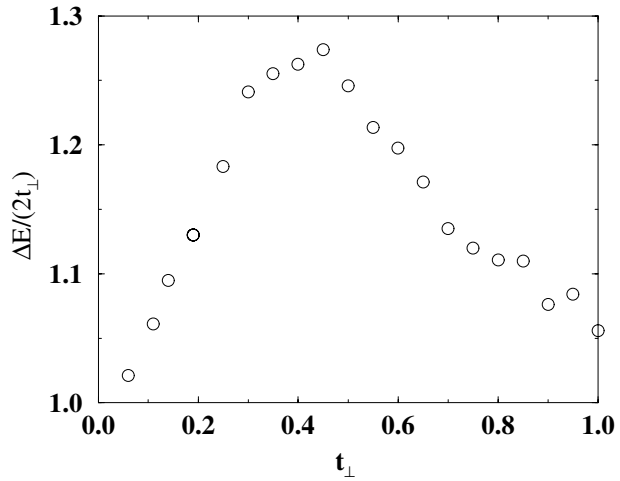

Figure 2. Splitting of the symmetric and the antisymmetric bands ΔE (in units of $2t_\perp$) versus $t_\perp$.

For small values of $t_\perp$ the band splitting $\Delta E/(2t_\perp)$ is around the unperturbed value of ≈ 1. However, with increasing $t_\perp$ it increases up to a maximum at $t_\perp \approx 0.4$. On further increasing $t_\perp$ the splitting is again reduced and eventually converges to the value of the non-interacting system $\Delta E/(2t_\perp) = 1$ again as $t_\perp \to \infty$.

The latter observation can be easily understood if one considers the limit $t_\perp/t \gg 1$. Here, we may consider each pair of opposite sites on the two layers as effectively decoupled from the rest of the system. In this case straightforward diagonalization of the remaining two-site cluster leads to the observed splitting $\Delta E = 2t_\perp$ in the Hubbard bands.

More astonishing and physically interesting is the fact that for moderate inter-layer coupling the effective hopping $t_\perp^{\mathrm{eff}}$ seems to be enhanced.

To shed more light on the physics behind that effect let us first consider the case of an additional antiferromagnetic exchange between the layers, $J_\perp > 0$. The development of the spectral functions with increasing $J_\perp$ is collected in figure 3, where on the right-hand side the details in the vicinity of the Fermi energy are shown.

With increasing $J_\perp$ the maximum of the symmetric band is shifted to higher energies while at the same time the position of the maximum of the antisymmetric band is moved to lower energies. For $J_\perp \approx 0.04$ the two maxima appear at the same energy. With further increasing $J_\perp$, the main weight of the antisymmetric band even shifts below that of the symmetric band and only a small shoulder around $\omega \approx \epsilon_- \approx -0.75$ indicates the original position of this band. Accordingly, the symmetric band has its main weight at higher energies than the antisymmetric band, again with a small shoulder at the original energy $\epsilon_+ \approx -1.5$.

A similar behaviour is also seen in the quasi-particle peak. However, the positions of the two peaks cross at a lower $J_\perp \approx 0.02$ and for the maximal value of $J_\perp = 0.1$ one can clearly

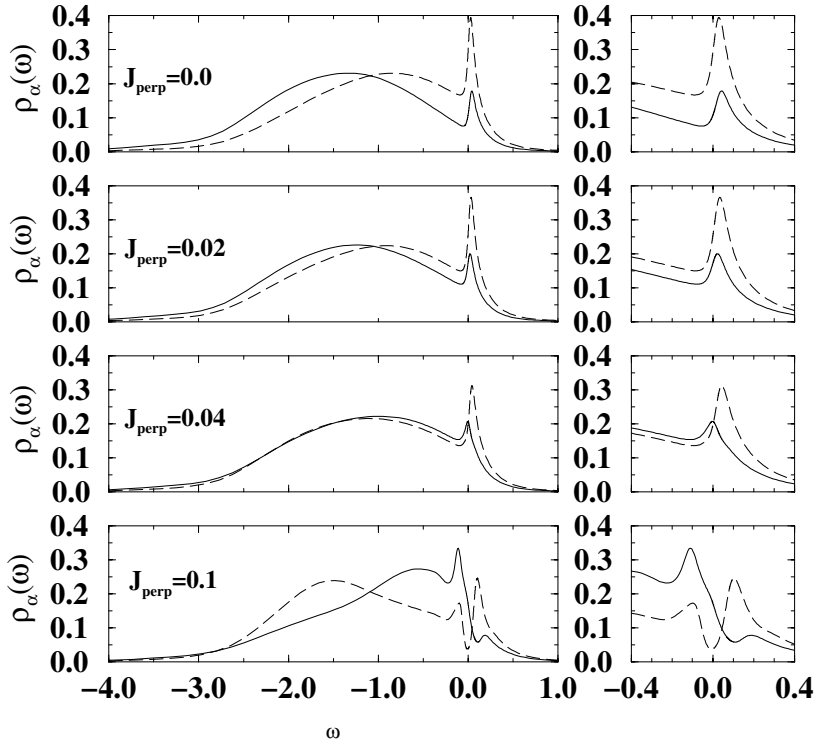

Figure 3. Spectral functions for the symmetric (solid line) and antisymmetric (dashed line) spectral functions with parameters $t_\perp = 0.2$, $\beta = 50.0$, $\delta = 0.05$ and various $J_\perp$: (a) $J_\perp = 0.0$, (b) $J_\perp = 0.02$, (c) $J_\perp = 0.04$, (d) $J_\perp = 0.1$. On the right-hand side the details around the Fermi level are shown.

distinguish two individual peaks in every band.

The movements of the peaks in the DOS represented by the positions of their maxima as a function of $J_\perp$ are collected in figure 4.

A simple explanation for the behaviour observed here can be given by neglecting the constraint of no double occupancy and treating the Hamiltonian $H_{J_\perp}$ in a standard mean-field factorization. This allows one to rewrite its contribution in the form of a hopping term. In this approximation the influence of $H_{J_\perp}$ reduces to a renormalization of the hopping to $t_\perp^{\mathrm{eff}} = t_\perp - \frac{1}{8} J_\perp \Delta n$, with $\Delta n = n_+ - n_-$. Since Δn of course depends on $t_\perp^{\mathrm{eff}}$ this must be read as a self-consistency equation. Note that $\Delta n > 0$; i.e. for $J_\perp > 0$ this renormalization always reduces $t_\perp$.

It is evident that such a simplified treatment will not reproduce the correct energy scales. Nevertheless we believe that it describes the observed behaviour of the spectral functions at least qualitatively, as it shows the renormalization of $t_\perp$ by $J_\perp$, namely a decrease of the renormalized inter-layer hopping including the change in sign for high enough values of $J_\perp$. Neglecting the usually positive sign of $J_\perp$ for the time being, one could also easily achieve $t_\perp^{\mathrm{eff}} > t_\perp$ by taking $J_\perp < 0$.

In connection with this observation it is interesting to note that for the case of $J_\perp = 0$ an inspection of the local two-particle states indicates that the $S = 1$ state is lowered in energy compared to the $S = 0$ state through the coupling to the effective medium. It thus seems that the system itself provides an effective ferromagnetic coupling between neighbouring spins on

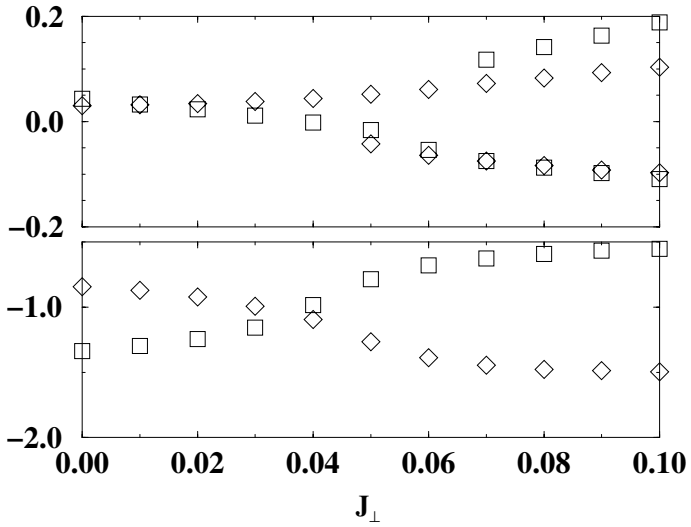

Figure 4. Maxima of the symmetric (squares) and antisymmetric (diamonds) spectral functions for various $J_\perp$. The lower part shows the lower Hubbard band; the upper part shows the region around the Fermi level.

different layers. With the above reasoning such a ferromagnetic coupling would consequently lead to $t_\perp^{\text{eff}} > t_\perp$ as $J_\perp \to 0$, which explains the enhancement observed in figure 2.

The remaining task thus is to understand the origin of the effective ferromagnetic coupling between the layers. Since we are dealing with a strongly correlated system close to half-filling we may approximate the situation as follows: the two opposing spins are coupled through a Kondo-type exchange coupling J_K to the effective medium in the corresponding layer, which in turn leads to a RKKY-like effective exchange coupling between the two spins $J_\perp^{\text{eff}} \propto -J_K^2 \cos(2k_{F\perp}r_\perp)/(k_{F\perp}r_\perp)^3$. Note that the actual sign of the effective coupling between local spins and the medium does not enter the argument. Since $k_{F\perp}$ is either 0 or $\pi/a_\perp$ and $r_\perp = a_\perp$, it follows that always $J_\perp^{\text{eff}} < 0$, i.e. it provides an effective ferromagnetic coupling between the layers.

Although the above argument is of course very hand-waving and has serious defects, further evidence for its qualitative correctness is obtained from an inspection of $\Delta E/(2t_\perp)$ as a function of the filling $\langle n \rangle$. For half-filling the system is an insulator and consequently no such $J_\perp^{\text{eff}}$ can exist, since it is based on the assumption of mobile particles. One thus would expect that for $\langle n \rangle \to 1$ one would obtain $\Delta E/(2t_\perp) = 1$ and observe an increase of $\Delta E/(2t_\perp)$ as $\langle n \rangle$ decreases. Such a behaviour can indeed be seen in figure 5, where the splitting ΔE versus the occupation number $\langle n \rangle$ is plotted for $t_\perp = 0.2$ and $J_\perp = 0.0$ and shows the anticipated initial rise. For still smaller particle numbers we expect a decrease of $\Delta E/(2t_\perp)$ again since the influence of correlations will be strongly reduced and the simple picture used in the explanation ceases to be valid. Unfortunately, the approximations in the NCA also break down for decreasing filling and $\langle n \rangle = 0.90$ was the lowest filling that we could reach with this method.

The last point that we want to discuss is the temperature dependence of the spectral functions. In figure 6 the spectral functions for various values of β are shown. On the left-hand side we consider the case for $J_\perp = 0.0$ while the right-hand side shows results for $J_\perp = 0.06$. The first interesting point here is that for the lower Hubbard bands the crossing of the two bands for finite values of $J_\perp$, as stated before and shown in figure 3, also strongly

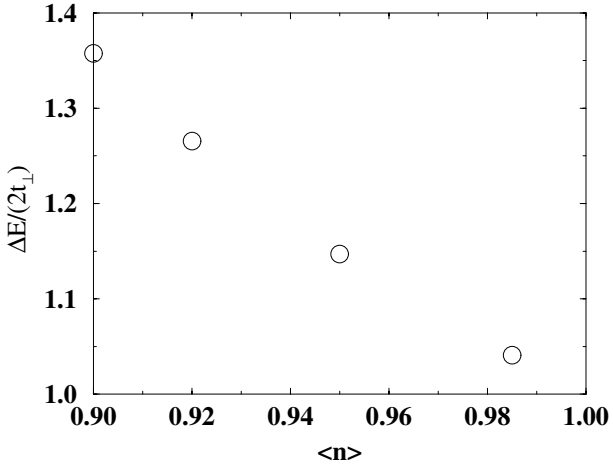

Figure 5. Splitting of the symmetric and the antisymmetric bands ΔE in units of $2t_\perp$ versus occupation number $\langle n \rangle$.

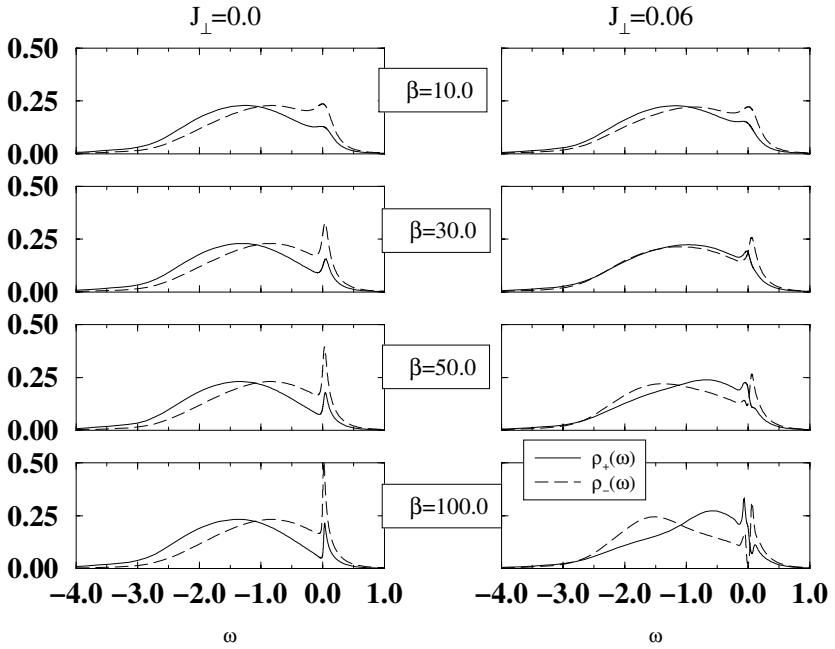

Figure 6. Temperature dependences of the spectral functions $\rho_+(\omega)$ (solid lines) and $\rho_-(\omega)$ (dashed lines). On the left-hand side results for $J_\perp = 0.0$ are shown; on the right-hand side we considered $J_\perp = 0.06$.

depends on temperature. Lowering the temperature for a fixed value of $J_\perp$ has similar effects to increasing $J_\perp$ for a fixed temperature. For $J_\perp = 0$, on the other hand, the positions of the maxima of the lower Hubbard bands appear to be almost insensitive to temperature.

This astonishing observation can be readily accounted for by the fact that for $\beta = 10, 30$ the temperature is higher than or of the order of $J_\perp = 0.06$ while it is lower for $\beta = 50, 100$. We thus expect that for the first two temperatures the local singlet–triplet splitting caused by

$J_\perp$ will be washed out due to temperature broadening, i.e. the effect on the Hubbard bands will be suppressed. It is interesting to note that for $\beta = 10$ the relative position of the maxima is even reversed as compared to that for $\beta = 100$, which can be understood with the help of an effective ferromagnetic exchange mediated by the medium, as discussed above. With decreasing temperature, on the other hand, the splitting due to $J_\perp$ becomes relevant, leading to the observed temperature dependence of the maxima of the lower Hubbard bands.

It is also very interesting to compare the development of the quasi-particle peaks at the Fermi level. As expected from their origin in a dynamically generated low-energy excitation similar to the Abrikosov–Suhl resonance, they are strongly temperature dependent. In contrast to the case for vanishing $J_\perp$, where they are at nearly the same energy for all temperatures, they show a similar behaviour at high temperatures but acquire well separated positions for low T as already stated earlier.

Let us summarize the previous discussion in a first important conclusion, namely that contrary to the initial expectations the effective band splitting in the bilayer t–J model is almost completely governed by magnetic correlations between neighbouring spins on different layers, whereas the correlations built in as the constraint of no doubly occupied sites seems to have, apart from giving rise to the usual formation of narrow quasi-particle bands at the Fermi level, only small influence.

4. Optical c-axis conductivity

As already pointed out by Clarke *et al* [7], the suppression of the coherent one-particle hopping in the normal state should manifest itself in the optical c-axis conductivity.

The optical c-axis conductivity $\sigma_c(\omega)$ is related to the current–current correlation function $\langle\langle j;\, j\rangle\rangle(\omega + \mathrm{i}\delta)$ by

$$\sigma_c(\omega) = -\frac{1}{\omega}\,\mathrm{Im}\langle\langle j;\, j\rangle\rangle(\omega + \mathrm{i}\delta). \tag{11}$$

The current operator in the c-direction

$$j = -\mathrm{i}t_\perp \sum_{\boldsymbol{k},\sigma} (a^\dagger_{+,\sigma}(\boldsymbol{k})a_{-,\sigma}(\boldsymbol{k}) - a^\dagger_{-,\sigma}(\boldsymbol{k})a_{+,\sigma}(\boldsymbol{k})) \tag{12}$$

can be derived from the continuity equation

$$j = \mathrm{i}[H,\, P] \tag{13}$$

as the time derivative of the c-component of the charge polarization

$$P = -\frac{1}{2}\sum_{\boldsymbol{k},\sigma} (a^\dagger_{+,\sigma}(\boldsymbol{k})a_{-,\sigma}(\boldsymbol{k}) + a^\dagger_{-,\sigma}(\boldsymbol{k})a_{+,\sigma}(\boldsymbol{k})). \tag{14}$$

In the two quantities the same combination of fermionic operators for the symmetric and antisymmetric bands occurs. This allows us to write the polarization–polarization correlation function $\langle\langle P;\, P\rangle\rangle$ as

$$\langle\langle P;\, P\rangle\rangle = \frac{1}{4}((\chi^{++} + \chi^{--}) + (\chi^{+-} + \chi^{-+})) \tag{15}$$

and $\langle\langle j;\, j\rangle\rangle$ as

$$\langle\langle j;\, j\rangle\rangle = t_\perp^2((\chi^{++} + \chi^{--}) - (\chi^{+-} + \chi^{-+})) \tag{16}$$

where the susceptibilities

$$\chi^{\alpha\kappa}(\mathrm{i}\nu_l) = \frac{1}{\beta^2}\sum_{\mathrm{i}\omega_n,\mathrm{i}\omega_m} \underline{\underline{\chi}}^{\alpha\kappa}(\mathrm{i}\nu_l) \tag{17}$$

have been introduced. $\underline{\underline{\chi}}^{\alpha\kappa}(\mathrm{i}\nu_l)$ is the shorthand matrix notation for the $\boldsymbol{q} = 0$ component of the (spatial Fourier transformed) particle–hole propagators

$$\begin{aligned}\left[\underline{\underline{\chi}}^{\alpha\kappa}_{i,j}(\mathrm{i}\nu_l)\right]_{nm} &= \chi^{\alpha\kappa}_{i,j}(\mathrm{i}\omega_n, \mathrm{i}\omega_m, \mathrm{i}\nu_l) \\ &= \sum_{\sigma,\sigma'} \frac{1}{\beta} \int_0^\beta \mathrm{d}\tau_1 \int_0^\beta \mathrm{d}\tau_2 \int_0^\beta \mathrm{d}\tau_3 \int_0^\beta \mathrm{d}\tau_4 \, \mathrm{e}^{-\mathrm{i}\omega_n(\tau_4-\tau_3)} \mathrm{e}^{-\mathrm{i}\omega_m(\tau_2-\tau_1)} \mathrm{e}^{-\mathrm{i}\nu_l(\tau_1-\tau_4)} \\ &\quad \times \langle T_\tau [a^\dagger_{\alpha,\sigma,i}(\tau_4) a_{\overline{\alpha},\sigma,i}(\tau_3) a^\dagger_{\overline{\kappa},\sigma',j}(\tau_2) a_{\kappa,\sigma',j}(\tau_1)] \rangle \end{aligned} \tag{18}$$

and $\mathrm{i}\omega_n$ and $\mathrm{i}\omega_m$ denote Fermi Matsubara frequencies and $\mathrm{i}\nu_l$ the external Bose Matsubara frequency. Here and in the following, the labels α, κ and γ denote the symmetric and anti-symmetric bands $\{+, -\}$, and $\overline{\alpha} = -\alpha$.

Using standard techniques [31], the susceptibilities can be expressed as functional derivatives of the Green's functions with respect to external fields according to the vertices. In this way one arrives at the following equations for the susceptibilities:

$$\underline{\underline{\chi}}^{\alpha\kappa}(\mathrm{i}\nu_l) = \delta_{\alpha,\kappa}\beta \underline{\underline{\chi}}^{\alpha\alpha(0)}(\mathrm{i}\nu_l) + \frac{1}{\beta} \sum_\gamma \underline{\underline{\chi}}^{\alpha\alpha(0)}(\mathrm{i}\nu_l) \underline{\underline{\Gamma}}^{\alpha\gamma} \underline{\underline{\chi}}^{\gamma\kappa}(\mathrm{i}\nu_l) \tag{19}$$

with

$$\left[\underline{\underline{\chi}}^{\alpha\alpha(0)}(\mathrm{i}\nu_l)\right]_{nm} = -\delta_{n,m} \sum_{\boldsymbol{k}} G_\alpha(\boldsymbol{k}, \mathrm{i}\omega_n + \mathrm{i}\nu_l) G_{\overline{\alpha}}(\boldsymbol{k}, \mathrm{i}\omega_n). \tag{20}$$

The two-particle self-energies $\underline{\underline{\Gamma}}^{\alpha\gamma}(\mathrm{i}\nu_l)$ are given as functional derivatives of the one-particle self-energies with respect to the local Green's functions. Because of the locality of the one-particle self-energies it follows that the two-particle self-energies are also purely local, and hence are identical to the two-particle self-energies of the effective impurity problem. This allows the calculation of the susceptibilities in a similar way to that described in [32, 33]. The important fact here is that we have four susceptibilities, which are not independent.

These four coupled Dyson equations for the susceptibilities are shown diagrammatically in figure 7. In this figure the upper left and right indices correspond to the labels α and κ of the susceptibilities in equation (19), while the lower labels are $\overline{\alpha}$ and $\overline{\kappa}$, respectively.

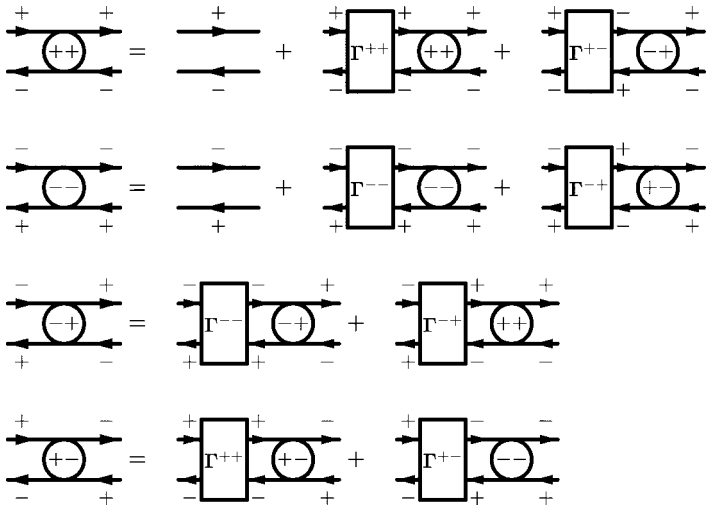

Figure 7. Dyson equations for the particle–hole propagators.

The Dyson equations for the local problem can be formulated with the same $\underline{\underline{\Gamma}}^{\alpha\gamma}$ by just replacing the susceptibilities $\underline{\underline{\chi}}^{\alpha\kappa}(\mathrm{i}\nu_l)$ for the lattice at $\boldsymbol{q} = 0$ by their local counterparts, $\underline{\underline{\chi}}^{\alpha\kappa}_{\mathrm{loc}}(\mathrm{i}\nu_l)$, i.e.

$$\underline{\underline{\chi}}^{\alpha\kappa}_{\mathrm{loc}}(\mathrm{i}\nu_l) = \delta_{\alpha,\kappa}\beta\underline{\underline{\chi}}^{\alpha\alpha\,(0)}_{\mathrm{loc}}(\mathrm{i}\nu_l) + \frac{1}{\beta}\sum_{\gamma}\underline{\underline{\chi}}^{\alpha\alpha\,(0)}_{\mathrm{loc}}(\mathrm{i}\nu_l)\underline{\underline{\Gamma}}^{\alpha\gamma}\underline{\underline{\chi}}^{\gamma\kappa}_{\mathrm{loc}}(\mathrm{i}\nu_l). \tag{21}$$

The local particle–hole propagators $\underline{\underline{\chi}}^{\alpha\kappa}_{\mathrm{loc}}$ can be calculated for the impurity by means of standard diagrammatic rules for the resolvent perturbation theory [22, 23], and since $\underline{\underline{\chi}}^{\alpha\alpha(0)}_{\mathrm{loc}}$ is expressed as

$$\left[\underline{\underline{\chi}}^{\alpha\alpha(0)}_{\mathrm{loc}}(\mathrm{i}\nu_l)\right]_{nm} = -\delta_{n,m}G_{\alpha}(\mathrm{i}\omega_n + \mathrm{i}\nu_l)G_{\bar{\alpha}}(\mathrm{i}\omega_n) \tag{22}$$

these equations can be solved for the unknown quantities $\underline{\underline{\Gamma}}^{\alpha\gamma}(\mathrm{i}\nu_l)$.

Inserting the solution for $\underline{\underline{\Gamma}}^{\alpha\gamma}(\mathrm{i}\nu_l)$ in equation (19) and solving it for $\underline{\underline{\chi}}^{\alpha\kappa}(\mathrm{i}\nu_l)$ finally leads to

$$\underline{\underline{\chi}}^{\alpha\alpha}(\mathrm{i}\nu_l) = \left[1 - (\underline{\underline{P}}^{\alpha\bar{\alpha}}\underline{\underline{P}}^{\bar{\alpha}\alpha})^{-1}\right]^{-1}\underline{\underline{M}}^{\alpha\alpha} \tag{23}$$

$$\underline{\underline{\chi}}^{\alpha\bar{\alpha}}(\mathrm{i}\nu_l) = (\underline{\underline{P}}^{\bar{\alpha}\alpha})^{-1}\underline{\underline{\chi}}^{\bar{\alpha}\bar{\alpha}} \tag{24}$$

with

$$\underline{\underline{M}}^{\alpha\alpha} = \left[(\underline{\underline{M}}^{\alpha\alpha}_{\mathrm{loc}})^{-1} - \frac{1}{\beta}\underline{\underline{\Theta}}\right]^{-1} \tag{25}$$

$$\underline{\underline{M}}^{\alpha\alpha}_{\mathrm{loc}} = \underline{\underline{\chi}}^{\alpha\alpha}_{\mathrm{loc}} - \underline{\underline{\chi}}^{\alpha\bar{\alpha}}_{\mathrm{loc}}(\underline{\underline{\chi}}^{\bar{\alpha}\bar{\alpha}}_{\mathrm{loc}})^{-1}\underline{\underline{\chi}}^{\bar{\alpha}\alpha}_{\mathrm{loc}} \tag{26}$$

$$\underline{\underline{P}}^{\alpha\bar{\alpha}} = \underline{\underline{\chi}}^{\alpha\alpha}_{\mathrm{loc}}(\underline{\underline{\chi}}^{\bar{\alpha}\alpha}_{\mathrm{loc}})^{-1}\underline{\underline{M}}^{\bar{\alpha}\bar{\alpha}}_{\mathrm{loc}}(\underline{\underline{M}}^{\bar{\alpha}\bar{\alpha}})^{-1}. \tag{27}$$

Complete information about the lattice is contained in the quantity

$$\underline{\underline{\Theta}}(\mathrm{i}\nu_l) = (\underline{\underline{\chi}}^{\alpha\alpha(0)}_{\mathrm{loc}}(\mathrm{i}\nu_l))^{-1} - (\underline{\underline{\chi}}^{\alpha\alpha(0)}(\mathrm{i}\nu_l))^{-1}. \tag{28}$$

The importance of the off-diagonal susceptibilities $\chi^{\alpha\bar{\alpha}}$ can be best seen by means of the exact relation

$$\langle\langle j; j\rangle\rangle(\mathrm{i}\nu_l) = (\mathrm{i}\nu_l)^2\langle\langle P; P\rangle\rangle(\mathrm{i}\nu_l) - t_{\perp}\,\Delta n \tag{29}$$

between the two correlation functions, which can be readily derived from the continuity equation (13), The difference of the occupation numbers $\Delta n = n_+ - n_-$ can be calculated from the single-particle spectral functions. Since it originates from a conservation law, equation (29) is intimately related to a Ward identity.

Since the $\underline{\underline{\Gamma}}^{\alpha\gamma}(\mathrm{i}\nu_l)$ are calculated from the local resolvents, this identity cannot be proven analytically, but has to be tested numerically. This can be seen in figure 8, where the l.h.s. and the r.h.s. of equation (29) are compared for $J_{\perp} = 0$ and different values of $t_{\perp}$ on the left-hand side and for different values of $J_{\perp}$ with a fixed value of $t_{\perp} = 0$ on the right-hand side. As all four susceptibilities are contained in $\langle\langle j; j\rangle\rangle(\mathrm{i}\nu_l)$ it is even non-trivial to consider just the case $\mathrm{i}\nu_l = 0$. Here $\langle\langle j; j\rangle\rangle(0)$ denotes the current–current correlation function calculated from the full equations for the static case $\mathrm{i}\nu_l = 0$, whereas for $\langle\langle j; j\rangle\rangle^0(0)$ the off-diagonal susceptibilities have been neglected.

This comparison also gives a crucial test for the calculation of the susceptibilities as it relates the simple quantity $t_{\perp}\,\Delta n$ calculated using the Green's functions to the susceptibilities obtained from the delicate calculation outlined above. It can be clearly seen that the inclusion of the off-diagonal susceptibilities is necessary to fulfil (29) and that the two quantities agree

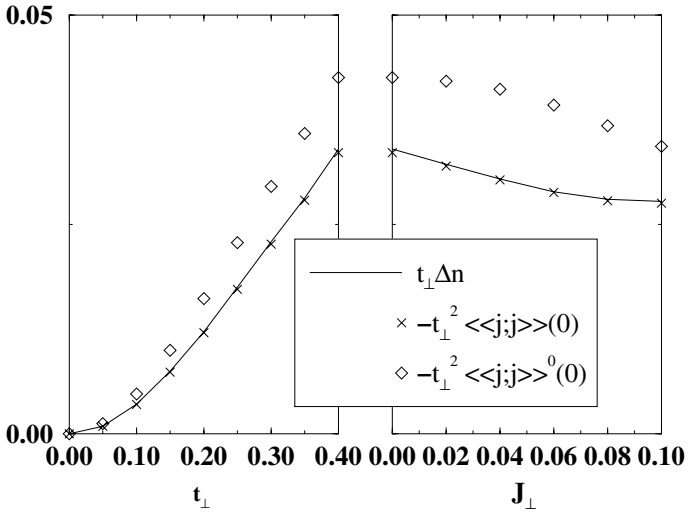

Figure 8. Comparison of the static current–current correlation function with ($\langle\langle j; j\rangle\rangle(0)$) and without ($\langle\langle j; j\rangle\rangle^0(0)$) the off-diagonal susceptibilities to $t_\perp\,\Delta n$, as a test for equation (29).

to a very high accuracy. We also checked the identity (29) for finite external frequencies $\mathrm{i}\nu_l$. Here the coincidence was less accurate but still satisfactory.

The analytic continuation of the susceptibilities to real frequencies was done with the Padé approximation [34]. Before looking at the results in detail, a remark about the low energy behaviour of the optical c-axis conductivity seems to be important. Since we consider a finite bilayer system in the c-direction where no charge transport with vanishing frequency is possible because of charge conservation, we do not expect a Drude peak. Thus the necessary relation $\sigma_c(0) = 0$ gives a further test for the numerical calculation and underlines the importance of the off-diagonal susceptibilities. While for $\sigma_c(0)$ calculated from $\sigma_c(\omega) = -\omega\,\mathrm{Im}\langle\langle P; P\rangle\rangle$ it is of course always fulfilled, equation (11) requires $\langle\langle j; j\rangle\rangle$ to vanish at least like ω^3 for $\omega \to 0$. In our calculations it was found that the latter behaviour was only achieved by the inclusion of the off-diagonal susceptibilities.

Results for the optical c-axis conductivity $\sigma_c(\omega)$ for various $t_\perp$ are shown in figure 9. The energy axis is in units of $2t_\perp$ to show the deviations of the peaks from their non-interacting values.

For large values of $t_\perp$ a narrow peak at $\omega \approx 2t_\perp$ is obtained. For $t_\perp \approx 0.5$ we find the position of the maximum of the optical c-axis conductivity to be above the value of $2t_\perp$ for free electrons. However, for small values of $t_\perp$ it can be seen that the charge response in the c-direction is strongly suppressed and only a broad featureless plateau is obtained, similar to what is indeed seen in optical experiments with multi-layer cuprates. Thus, for the optical c-axis conductivity the strong correlations in the form of the Coulomb repulsion appear to have a quite drastic effect especially for small $t_\perp$. Note that this observation is not apparent from the single-particle DOS, where the behaviour is rather consistent with a conventional band splitting. Therefore, our results also underline the fact that one has to be very careful in drawing conclusions about two-particle properties on the basis of the behaviour of one-particle quantities alone.

The optical c-axis conductivity for $J_\perp = 0.0$ and varying doping in figure 10 also shows a strong suppression when approaching half-filling $\delta = 0.0$. This is clear, as for $\delta \to 0$ the constraint of no double occupancy simply inhibits any transport. In addition to this it can also

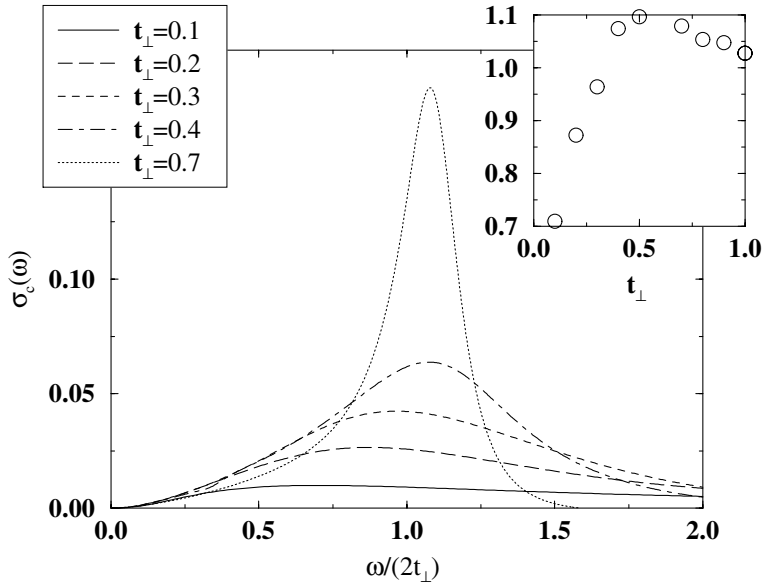

Figure 9. Optical c-axis conductivity for $J_\perp = 0.0$ and doping $\delta = 0.05$ and various $t_\perp$ versus frequency ω in units of $2t_\perp$. The inset shows the position of the peaks in units of $2t_\perp$ versus $t_\perp$.

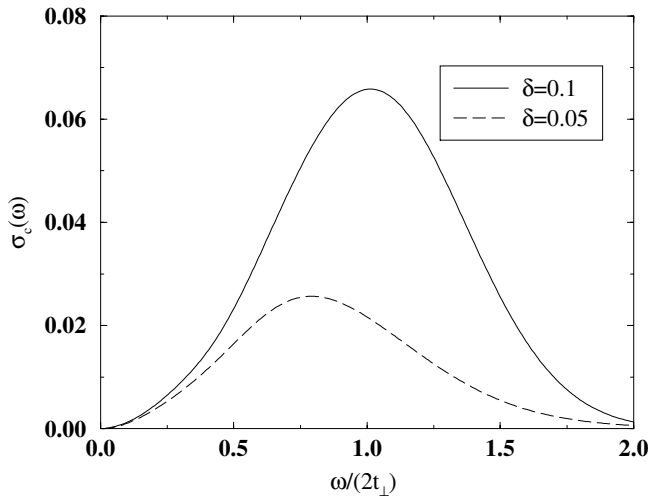

Figure 10. Optical c-axis conductivity for $t_\perp = 0.2$, $J_\perp = 0.0$ and various dopings δ.

be seen that the position of the peak is shifted to lower energies for constant $t_\perp$.

A finite value of $J_\perp$ further enhances this effect, as can be seen from figure 11. For $J_\perp = 0.0$ up to $J_\perp = 0.04$ the charge-fluctuation peak is shifted to lower energies and the height of the peak decreases. On further increasing $J_\perp$ a new peak emerges at low energies. This new peak slightly shifts to higher energies and grows with increasing $J_\perp$. The physical origin for these low-energy excitations is inter-plane spin excitations, and consequently the new peak is of similar nature to a peak in the in-plane optical conductivity of the one-band t–J model observed in the parameter regime $J = 1.5$–2.0 and scaling with J [35, 36].

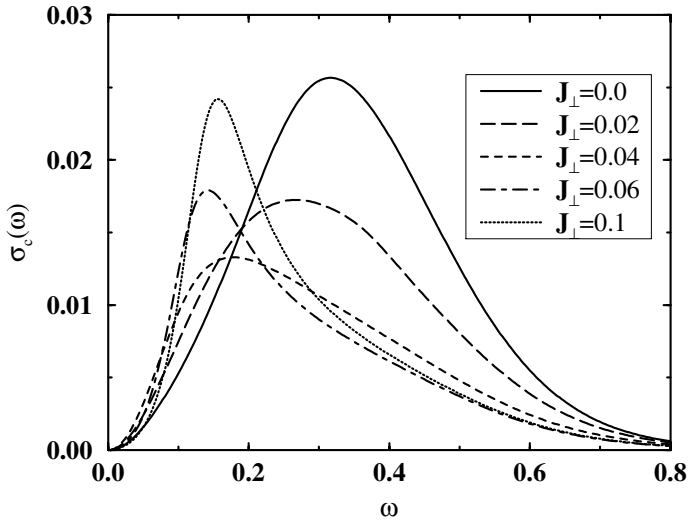

Figure 11. Optical c-axis conductivity for $t_\perp = 0.2$, $\delta = 0.05$ and various $J_\perp$.

The strong relationship of this peak with the many-body resonance in the spectral functions can be seen by looking at $\sigma_c(\omega)$ for $t_\perp = 0.2$ and different values of the inverse temperature β shown in figure 12. Here we also compare the cases $J_\perp = 0.0$ on the left-hand side and $J_\perp = 0.06$ on the right-hand side as for the spectral functions in figure 6.

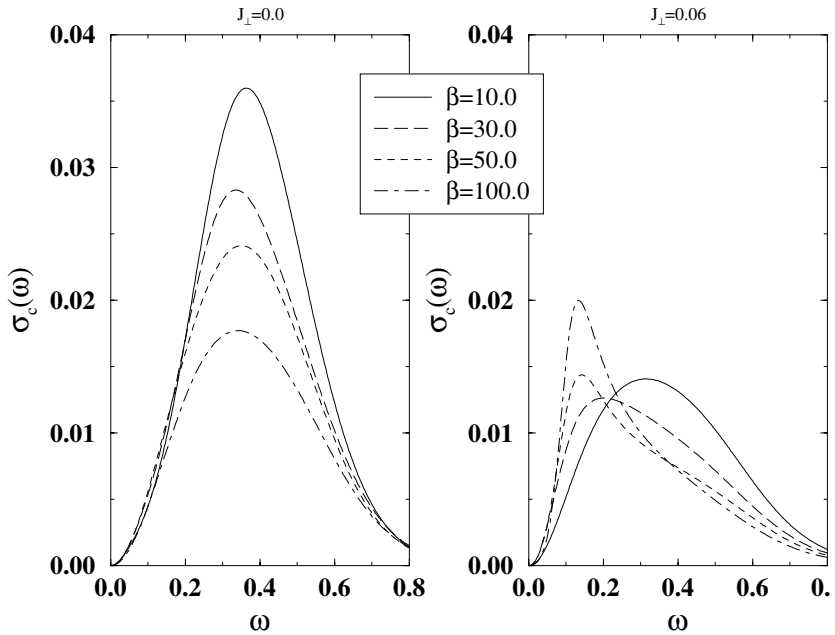

Figure 12. Optical conductivity for $t_\perp = 0.2$, $J_\perp = 0.06$, $\delta = 0.05$ and various β. As in figure 6, on the left-hand side results for $J_\perp = 0.0$ are shown, while on the right-hand side we considered $J_\perp = 0.06$.

For $J_\perp = 0.0$ the optical conductivity just has a charge-fluctuation peak at around $2t_\perp$. The height of this peak is reduced for decreasing temperature, but despite the emerging of the Kondo-like peaks at the Fermi level, as seen on the left-hand side of figure 6, no pronounced low-energy excitation in the optical conductivity can be seen. If we compare this to the case of $J_\perp = 0.06$ on the right-hand side of figure 12, we again see a suppression of the height of the peak at $\omega \approx 2t_\perp$ on lowering the temperature. But as with increasing β the quasi-particle peaks in the spectrum start to grow and move apart (see figure 6, right-hand side), the spectral weight in the optical conductivity is shifted to lower energies and a new peak emerges at $\omega \approx 2J_\perp$. Let us stress again that the decisive difference compared to the case of $J_\perp = 0.0$ is the splitting of the Kondo-like peaks at the Fermi level, which scales with $J_\perp$ rather than $t_\perp$. Because of the temperature dependence and the intimate connection with $J_\perp$, it can be concluded that this excitation in the optical conductivity must be attributed to low-energy excitation with a $J_\perp$-dependent energy scale.

5. Summary and conclusions

In this work we investigated a bilayer model with strong electronic correlations and presented results for the one-particle properties and the optical conductivity perpendicular to the planes connected with charge fluctuations between the layers. The model was solved within the dynamical mean-field theory with special emphasis on the coupling between the planes, particularly the antiferromagnetic coupling $J_\perp$. For $J_\perp = 0.0$ we found an enhancement of the one-particle hopping between the planes, which may be attributed to ferromagnetic correlations, whereas for $J_\perp > 0$ a strong suppression can be found, up to a complete blocking of the inter-planar charge dynamics for intermediate values of $J_\perp$. Corresponding effects could also be found in the analysis of the optical conductivity in the c-direction, where a suppression of the charge dynamics by strong correlations is found. For moderate values of $t_\perp$ we observed a rather featureless optical conductivity in the c-direction, which is in qualitative accordance with experiments for the cuprates. The influence of $J_\perp$ was found to further lower the strength and to shift the response to lower energies. For larger values of $J_\perp$ a peak appears which scales with $J_\perp$ and increases with decreasing temperature. This peak can be attributed to spin fluctuations and is expected to be found also in the inter-plane magnetic susceptibility. In summary it can be said that for finite but not too high values of $J_\perp$ the coherent one-particle hopping between the planes of the two layers is suppressed as can be seen in the splitting of the symmetric and antisymmetric bands and in the optical conductivity.

Acknowledgment

This work was partially supported by the DFG grant PR 298/5-1.

Appendix A. The double-impurity Anderson model

In this paper we applied the DMFT to a double-layer system, choosing as local unit a two-site molecule coupled to two effective media of conduction electrons on the two layers. The local problem was solved using a perturbation theory in the hybridization interaction within the so-called non-crossing approximation (NCA). In this appendix we want to discuss the accuracy of this approximation by comparing results for a double-impurity Anderson model (DIAM) with a single-impurity Anderson model (SIAM) in a special limit.

For the double-impurity system coupled to two bands of conduction electrons we use the following Hamiltonian:

$$H = \sum_{\alpha,\boldsymbol{k},\sigma} \epsilon_{\alpha,\boldsymbol{k}} c^{\dagger}_{\alpha,\boldsymbol{k},\sigma} c_{\alpha,\boldsymbol{k},\sigma} + \sum_{\alpha,\sigma} \epsilon_{\alpha} f^{\dagger}_{\alpha,\sigma} f_{\alpha,\sigma} + V \sum_{\boldsymbol{k},\alpha,\sigma} (f^{\dagger}_{\alpha,\sigma} c_{\alpha,\boldsymbol{k},\sigma} + \text{h.c.}) - t_{\perp} \sum_{\sigma} (f^{\dagger}_{1,\sigma} f_{2,\sigma} + f^{\dagger}_{2,\sigma} f_{1,\sigma}) - J_{\perp} \boldsymbol{S}^{f}_{1} \cdot \boldsymbol{S}^{f}_{2}. \tag{A.1}$$

For the density of states of the conduction electrons we use $\rho_{\alpha}(\omega) = \rho_0 \Theta(D - |\omega|)$ and measure all energies in units of the Anderson width $\Delta = \pi \rho_0 V^2$.

The model (A.1) has the property that in the limit $t_{\perp} \to 0$ and accordingly $J_{\perp} \to 0$ it describes two identical single impurities coupled to separate conduction bands. The result for the partition function should therefore factorize into the product of two partition functions for single impurities in this limit, and the single-particle Green's function should be identical for the DIAM and the SIAM. This is not the case, if we treat the double-impurity model in the NCA. Before we discuss the reason for this discrepancy in detail, let us look at some numerical results for the local Green's function.

In figure A1 we show results for the spectral function calculated for the DIAM and the SIAM within the NCA for $t_{\perp} = 0$, $J_{\perp} = 0$ and model parameters $\epsilon_f = -3$, $\beta = 100$.

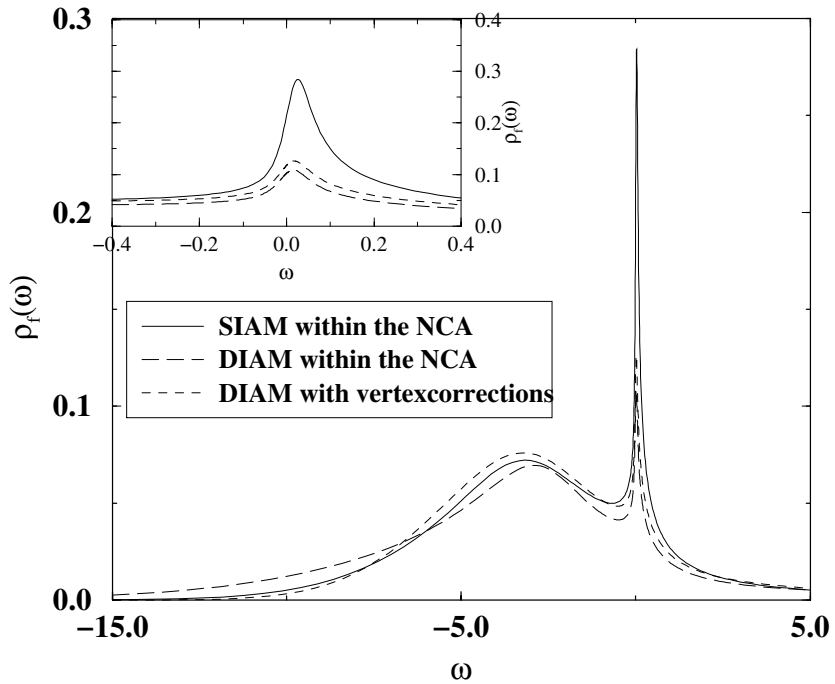

Figure A1. Comparison of the resolvent techniques for the SIAM and the DIAM. The solid line shows the spectral function for the SIAM calculated with the NCA. The dotted line shows the spectral function for the DIAM calculated within the NCA, and the dashed line shows the result for the DIAM achieved by including vertex corrections. The inset shows the details around the Fermi level.

Although the qualitative features are similar, the two results do not agree completely: in the DIAM the charge-fluctuation peak is slightly broader, but, more important, the Kondo peak is lower. The difference is due to the NCA used. In fact, the discrepancy can be reduced,

if vertex corrections beyond the NCA are included for the DIAM, as becomes evident from figure A1.

The reason why the NCA works differently for two decoupled impurities and for a double-impurity model with $t_\perp = 0$ can be understood best with the help of the diagrams for the partition function. Since the inclusion of the two-particle interaction into the unperturbed part of the Hamiltonian forbids the use of Wick's theorem, the resolvent technique works with time-ordered Green's functions. In the case of two single impurities we have separate time integrations for each impurity. A second-order correction for the first impurity due to the hybridization with $\tau_2 > \tau_1$ is given by the diagram shown in figure A2(a) and a fourth-order diagram for the second impurity with $\tau_6 > \tau_5 > \tau_4 > \tau_3$ is shown in figure A2(b).

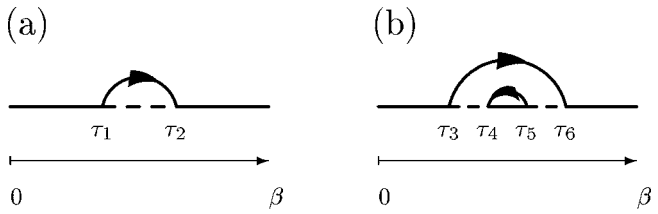

Figure A2. Diagrams for the decoupled impurities.

Within a resolvent perturbation theory for the DIAM the individual contributions in figure A2 will lead to several possible diagrams shown in figure A3. In the case of $\tau_1 > \tau_6$ we obtain the diagram in figure A3(a), whereas for $\tau_6 > \tau_2 > \tau_5 > \tau_4 > \tau_1 > \tau_3$ the diagram is like that in figure A3(b). These two diagrams have in common that they are included in the standard NCA for the DIAM. But other possible time orderings are given by $\tau_2 > \tau_6 > \tau_1 > \tau_5 > \tau_4 > \tau_3$ where the resulting diagram is shown in figure A3(c), and $\tau_2 > \tau_6 > \tau_5 > \tau_1 > \tau_4 > \tau_3$ as shown in figure A3(d). Diagrams of the type figure A3(c) are included in the treatment of the DIAM with vertex corrections, leading to the improvement visible in figure A1. Diagrams like the one in figure A3(d) are responsible for the remaining differences. Including these types of diagram, and even higher-order vertex corrections, would impose numerical complications that are beyond all technical possibilities.

This example already shows that in order to obtain the same level of accuracy in the DIAM

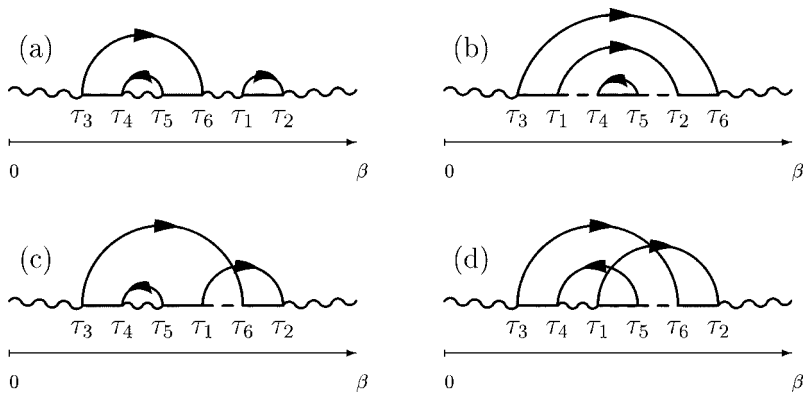

Figure A3. Diagrams for the DIAM which result of the combination of the diagrams for the single impurities in figure A2.

in comparison with the SIAM, vertex corrections up to infinite order have to be included in principle. As, however, the main features of the spectral function are already well described by the NCA for the DIAM, we neglect the numerical cumbersome and time-consuming vertex corrections in our calculations. Besides this, it can be expected that the vertex corrections become much less important in the lattice problem as the coupling of the impurity to the conduction bands of the order of $t/t_\perp$ becomes smaller with increasing $t_\perp$.

References

[1] Hubbard J 1963 *Proc. R. Soc.* A **276** 238
Gutzwiller M C 1963 *Phys. Rev. Lett.* **10** 159
Kanamori J 1963 *Prog. Theor. Phys.* **30** 257
[2] Zhang F C and Rice T M 1988 *Phys. Rev.* B **37** 3759
[3] Chao K A, Spalek J and Oles A M 1977 *J. Phys. C: Solid State Phys.* **58** L271
[4] Hirsch J E 1985 *Phys. Rev. Lett.* **54** 1317
[5] Dagotto E 1994 *Rev. Mod. Phys.* **66** 763
[6] Chakravarty S, Sudbø A, Anderson P W and Strong S 1993 *Science* **261** 337
[7] Clarke D G, Strong S P and Anderson P W 1995 *Phys. Rev. Lett.* **74** 22
[8] Campuzano J C *et al* 1990 *Phys. Rev. Lett.* **64** 2308
[9] Liu R, Veal B W, Paulikas A P, Downey J W, Kostić P J, Fleshler S, Welp U, Olson C G, Wu X, Arko A J and Joyce J J 1992 *Phys. Rev.* B **46** 11 056
[10] Ding H, Bellman A F, Campuzano J C, Randeria M, Norman M R, Yokoya T, Takahashi T, Katayama-Yoshida H, Mochiku T, Kadowaki K, Jennings G and Brivio G P 1996 *Phys. Rev. Lett.* **76** 1533
[11] Shen Z X and Dessau D S 1995 *Phys. Rep.* **253** 1
[12] Holmes C C, Timusk T, Liang R, Bonn D A and Hardy W N 1993 *Phys. Rev. Lett.* **71** 1645
[13] Dahm T, Manske D and Tewordt L 1996 *Phys. Rev.* B **54** 6640
[14] Liechtenstein A I, Gunnarson O, Andersen O K and Martin R M 1996 *Phys. Rev.* B **54** 12 505
[15] Grabowski S, Schmalian J, Langer M and Bennemann K H 1997 *Phys. Rev.* B **55** 2784
[16] Tranquada J M 1992 *Phys. Rev.* B **46** 5561
[17] Metzner W and Vollhardt D 1989 *Phys. Rev. Lett.* **62** 324
[18] Müller-Hartmann E 1989 *Z. Phys.* B **74** 507
[19] Pruschke Th, Obermeier Th, Keller J and Jarrell M 1996 *Physica* B **223+224** 611
[20] For a review, see Georges A, Kotliar G, Krauth W and Rozenberg M J 1996 *Rev. Mod. Phys.* **68** 13
[21] Kim C-J, Kuramoto Y and Kasuya T 1987 *Solid State Commun.* **62** 627
[22] Keiter H and Kimball J C 1971 *Int. J. Magn.* **1** 233
[23] Keiter H and Morandi G 1984 *Phys. Rep.* **109** 227
[24] Bickers N E, Cox D L and Wilkins J W 1987 *Phys. Rev.* B **36** 2036
[25] Obermeier Th, Pruschke Th and Keller J 1996 *Ann. Phys., Lpz.* **5** 137
[26] Pruschke Th, Jarrell M and Freericks J K 1995 *Adv. Phys.* **44** 187
[27] Pruschke Th, Cox D L and Jarrell M 1993 *Phys. Rev.* B **47** 3553
[28] Schmalian J, Lombardo P, Avignon M and Bennemann K H 1996 *Physica* B **223+224** 602
Lombardo P, Avignon M, Schmalian J and Bennemann K H 1996 *Phys. Rev.* B **54** 5317
[29] Schork T and Blawid S 1997 *Phys. Rev.* B **56** 6559
[30] Maier Th, Zölfl M B, Pruschke Th and Keller J 1999 *Eur. Phys. J.* B **7** 377
[31] Brandt U and Mielsch C 1998 *Z. Phys.* B **75** 365
[32] Pruschke Th, Qin Q, Obermeier Th and Keller J 1996 *J. Phys.: Condens. Matter* **8** 3161
[33] Pruschke Th, Obermeier Th and Keller J 1996 *Physica* B **230–232** 895
[34] Vidberg H J and Serene J W 1977 *J. Low Temp. Phys.* **29** 179
[35] Eder R, Wróbel P and Ohta Y 1996 *Phys. Rev.* B **54** 11 034
[36] Vojta M and Becker K W 1998 *Eur. Phys. J.* B **3** 427